

**GT2022-81777**

**AERODYNAMIC DAMPING OF COMPOSITE UHBR FANS UNDER THE  
CONSIDERATION OF ACOUSTIC INTAKE REFLECTIONS**

**Jan Goessling\***  
**Joerg R. Seume**

Institute of Turbomachinery and Fluid Dynamics  
Leibniz University Hannover  
30823 Garbsen  
Germany  
Email: goessling@tfd.uni-hannover.de

**Jan Peter Flüh**  
**Nicola Paletta**

IBK Innovation GmbH & Co. KG  
21129 Hamburg  
Germany  
Email: nicola.paletta@ibk-innovation.de

**Torben Eggers**  
**Jens Friedrichs**

Institute of Jet Propulsion and Turbomachinery  
Technische Universität Braunschweig  
38108 Braunschweig  
Germany  
Email: t.eggers@ifas.tu-braunschweig.de

**Nunzio Natale**

DREAM INNOVATION Srl  
81030 Sant'Arpino  
Italy  
Email: nunzio.natale@dreaminnovation.it

**ABSTRACT**

*Steadily rising regulations and demands on aeroengines require the continuous reduction of CO<sub>2</sub> emissions. Among other factors, particularly the weight reduction of the engine as well as synergetic engine-airframe integration are of major concern. Both lead to the application of shorter and more sensitive intakes as well as new materials, such as fiber composites. Fiber composites generally have a considerably lower density but a similar stiffness compared to common fan blade materials resulting in a reduction of the engines' weight. A further difference from conventional materials is the anisotropic behavior of the stiffness, imposed by the ply orientation. In this paper, the impact of the use of fiber composites for the scaled rotor of an ultra-high bypass ratio (UHBR) fan on the aeroelasticity is investigated numerically. In order to influence the eigenfrequency and mode shape, the ply orientation of the blade lay-up is varied.*

*The influence on the resulting aerodynamic damping is analyzed numerically, using a harmonic balance approach. For an accurate prediction, the aeroacoustic reflection at the intake highlight plane is incorporated in the numerical model and its impact is quantified for different intake lengths. The results are compared to a titanium alloy blade design (Ti-6Al-4V) and show the capability of varying the eigenfrequency with a coupled change in twist-to-plunge ratio due to lay-up variations. This change of the structural dynamics of the rotor blade influences the aerodynamic damping. Additionally, acoustic reflections are found to affect the stability, depending on the lay-up, operating condition, and intake length. A lay-up was found, which stabilizes the fan blade for all investigated conditions operating with a typical short ultra-high bypass ratio (UHBR) intake. A special lay-up generates negative aerodynamic damping of -6.6% (logarithmic decrement) when operated close to stall. This fulfills the present project's particular need to measure flutter in a wind tunnel.*

\*Address all correspondence to this author.

## NOMENCLATURE

### Symbols

$c$	blade chord length
$d$	diameter
$\hat{d}$	vibrational amplitude
$E_{modal}$	modal energy
$f$	blade eigenfrequency
$k$	reduced frequency
$l$	intake length
$\dot{m}$	mass flow
$M_{modal}$	modal mass
$Ma$	Mach number
$n$	rotational speed
$N$	number of nodes
$p$	pressure
$r$	radius
$T$	temperature
$u$	flow velocity relative the blade
$W_{cyc}$	aerodynamic work per cycle
$x$	deformation vector
$\alpha$	twist-to-plunge ratio
$\beta, \beta'$	velocity flow angle
$\delta$	logarithmic decrement
$\phi$	phase of acoustic wave
$v$	hub-to-tip ratio
$\omega$	angular frequency

### Subscripts

$a^H$	hermitian adjoint of $a$
$\hat{a}$	amplitude of quantity $a$
$\tilde{a}$	complex amplitude of quantity $a$
$ax$	axial direction
$LE$	leading edge
$TE$	trailing edge
$t$	total quantity
$\ominus$	circumferential

<b>CFD</b>	computational fluid dynamics
<b>CFPR</b>	carbon fiber reinforced polymers
<b>DLR</b>	German Aerospace Center
<b>EO</b>	engine order
<b>GCI</b>	grid convergence index
<b>HB</b>	harmonic balance
<b>MPC</b>	multi-point-constraint
<b>ND</b>	nodal diameter
<b>RANS</b>	Reynolds-averaged Navier–Stokes
<b>UHBR</b>	ultra-high bypass ratio

## INTRODUCTION

The current trend to increase the propulsive efficiency of modern aero engines is to increase the bypass mass flow rate and

decrease nozzle exit velocity using UHBR fan designs. To reduce the weight of the enlarged fan, the use of lighter and stiffer materials for the blades, such as carbon fiber reinforced polymers (CFPR), and shorter intake designs are necessary. Both play an important role in the aeroelastic stability of such low transonic fans and need to be carefully considered during the design process of a composite UHBR fan.

Flutter is of major concern for these fans, operated in the flat part of the compressor characteristic [1]. Flutter is a self-excited vibration, where energy of the flow is transformed in blade vibration due to interactions of the vibration itself and the caused unsteady aerodynamic pressure on the blade surface; leading to positive or negative (flutter) aerodynamic damping. The vibration is non-synchronous with the engine order (EO). For fan blades, two mechanism cause flutter; stall flutter and acoustic driven flutter [2]. Several studies in the past decade have analyzed the phenomena stall flutter and identified different important parameters for fan blades. In most cases stall flutter occurs for the 1st flap mode (1F), vibrating in the 1st to 6th nodal diameter (ND). This phenomena is driven by a separated region and radial mitigation on the suction surface of the blade [3]. For the rotor-only aerodynamic damping, the reduced frequency and mode shape drive the sensitivity of the blade design to stall flutter, as shown in [4]. The reduced frequency is defined as

$$k = 2\pi \frac{fc}{u}, \quad (1)$$

including the blade frequency  $f$ , the chord length  $c$  and the flow velocity relative to the blade  $u$ . Reduced frequencies  $k < 0.8$  for the first bending mode are prone to flutter [4]. A common parameter to describe the mode shape and its influence on the flutter stability is the twist-to-plunge ratio. This ratio is calculated as

$$\alpha = \frac{2(\hat{x}_{LE} - \hat{x}_{TE})}{\hat{x}_{LE} + \hat{x}_{TE}}, \quad (2)$$

where  $\hat{x}_{LE}$  is the deformation at the leading edge and  $\hat{x}_{TE}$  is the deformation at the trailing edge of the mode shape. A higher twist component favors the flutter instability, since the lift fluctuation due to twist is always negatively damping, as shown in [5] and [1]. In [6], a stability line over reduced frequency and twist-to-plunge ratio is given for fan blade flutter. The cut-on condition of the acoustic modes induced by the blade vibration up- and downstream of the rotor is a flutter constrain. Flutter can occur if the vibration frequency and operating conditions (Mach number, swirl, etc.) fulfill the cut-on condition for upstream propagating waves, but waves propagating downstream behind the rotor are cut-off [2]. For this condition, the initially downstream propagating pressure wave sends pressure waves upstream through the blade passage. These interact with the leading edge pressure, influencing the work done and thus the aerodynamic damping.

In addition to stall flutter, acoustic driven flutter is a critical mechanism for the stability of fan blades. In combination with low rotor-only damping at throttled fan condition, the acoustic reflection at the intake lip can reduce the damping critically such that flutter occurs. This is often referred to as "flutter bite", e.g. [7]. For acoustic driven flutter, upstream propagating acoustic waves are reflected on the intake highlight due to the impedance discontinuity between intake duct and far field. The reflected wave travels downstream and superposes with the unsteady pressure field on the rotor blade, [2]. The change of unsteady pressure on the blade surface has either a stabilizing or destabilizing effect on the aerodynamic damping. This is dependent on the phase of the reflected wave close to the rotor and the most destabilizing case is, when the upstream wave lags the reflected wave by  $90^\circ$ . Different analytical and numerical approaches to predict and quantify the effect of intake reflections on fan blade flutter are given in the literature [8–10].

A general approach to improve the stall flutter stability is to increase the blade eigenfrequency and adapt the torsional axis [11]. This is also applicable for fan blade flutter [6]. For conventional materials, this requires a redesign of the blade geometry. In addition, the usage of intentional mistuning is increasing the blade stability [12]. In [13], two methods to increase blade stability have been analyzed: the change of the steady aerodynamic loading distribution of the blade and the alternation of the unsteady pressure propagation. For acoustic driven flutter, the change of the intake length can increase the flutter stability, as shown in [1]. The use of a 3.5 times extended intake moves the theoretical flutter bite to such low rotational speeds, that the upstream acoustic mode is cut-off and damped. This leads to the suppression of the flutter bite, however such long intake is not practical for real engines. The authors also investigate the use of acoustic liners to increase the flutter stability, but found that these are only effective for high-speed fans.

In addition to the advantage of composite materials being lighter and stiffer compared to the titanium alloy materials, the use of composite materials allows the variation of structural blade behavior without the need to change the blade geometry itself. The potential to influence the rotor-only aerodynamic damping and to stabilize composite fan blades with different composite lay-ups is shown in [14]. However, the studies do not consider intake reflection causing acoustic flutter.

Therefore, this paper analyzes different composite blade designs regarding the aerodynamic damping and flutter stability of coupled intake and rotor. The coupled results are also compared to rotor-only damping. By modifying the orientation of the plies within the lay-up, a wide range of eigenfrequencies and twist-to-plunge ratios can be served. This is used to generate a composite blade design stable for all operating points. For the special requirements of the CA3ViAR project, a lay-up that generates unstable operating condition to measure flutter instabilities is presented and analyzed.

**TABLE 1. FAN DESIGN PARAMETERS**

	Rig (sea level)	
	Cruise	Take-Off
Operating point		
Bypass ratio	17	15.8
Mach number $Ma_{ax}$	0.62	0.52
Mass flow $\dot{m}$ / (kg/s)	63.39	57.15
Rot. speed $n$ / RPM	8667	8095
Fan tip speed $V_\Theta$ / (m/s)	295	275
Scale factor	1:3.3	
Fan tip radius $r_{tip}$ / m	0.325	
Hub-to-tip ratio $\nu$	0.26	
No. of rotor blades	18	
No. of stator blades	40	

## FAN DESIGN INVESTIGATED

The fan design analyzed in this work is based on the scaled UHBR fan stage of a turbofan engine within the CA3ViAR project ensuring Mach number and geometrical similarity [15]. The project aims to design a composite rotor, which features aerodynamic and aeroelastic instabilities at off-design conditions. The fan stage will be tested within the project regarding its aerodynamic, aeroelastic, and aeroacoustic behavior. The results will be published as an open-test case. Important fan design parameters are given in Tab. 1. Further information about the fan design process and the preliminary design are given in [15] and [16]. The fan design in this work deviates from the earlier published design by reducing the blade curvature at the foot, adding  $8^\circ$  positive lean towards the suction side and reducing the camber. The running tip clearance is increased from 0.5 mm to 0.75 mm. The rotor is shifted 5 mm downstream. The stator design remains the same. The airfoil section of the reference and the design analyzed in this work are shown in Fig. 1. Figure 2 shows the fan performance map of the current design with short intake. Typical for higher bypass ratio engines with constant nozzle design, the take-off and approach operating points of the fan move closer to the part-power limit, hence reducing its stall margin and increasing the risk of fan flutter [17]. The stalling mechanism is fan-driven, mainly due to separation near the blade tip. The total pressure ratio is calculated between the interface 3-I and the outlet 5, defined in Fig. 3. The choke line is not fully resolved since this study is analyzing flutter close to the stall line mainly induced by acoustic reflection at the intake highlight. The throttled condition at design speed (8667 RPM)

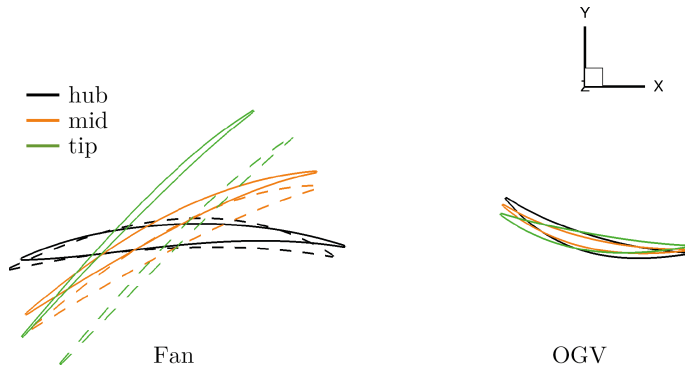


**FIGURE 1.** AIRFOIL SECTIONS OF THE FAN STAGE, SOLID: USED IN THIS WORK, DASHED: REFERENCE [15]

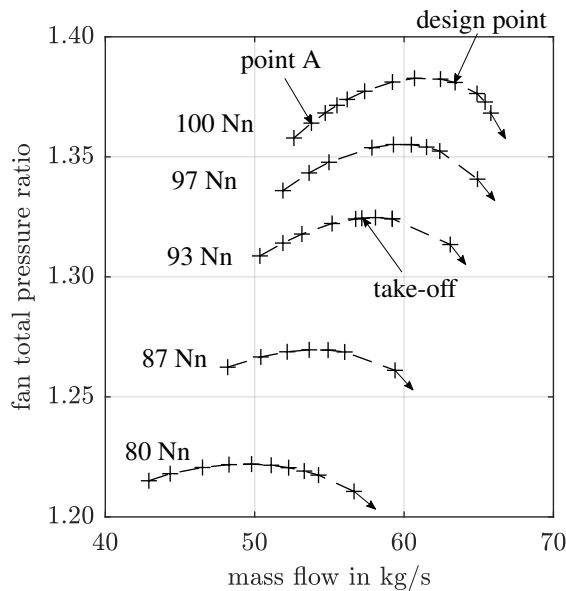


**FIGURE 2.** PERFORMANCE MAP OF INVESTIGATED FAN DESIGN

with 53.8 kg/s mass flow rate, marked as point A, is analyzed in detail within this work. This is the point with the lowest expected aerodynamic damping with intake length to diameter of  $l/d = 0.36$ .

## COMPUTATIONAL APPROACH

### CFD approach

The flutter simulations of the different composite blade designs are performed with the nonlinear research solver *TRACE* harmonic balance (HB) developed by the German Aerospace Center (DLR). The solver computes the unsteady Reynolds-averaged Navier–Stokes (RANS) equations in the frequency do-

main assuming that Fourier series can represent the unsteady part. The solver and the method used is described in detail by [18] and [19]. The mode shape is mapped on the computational fluid dynamics (CFD) mesh with a constant vibrating amplitude, inducing the unsteady pressure field at the specific frequency. The mapped amplitude is  $\hat{d} = 0.1$  mm at the point with maximum modal displacement. The aerodynamic damping is described with the logarithmic decrement, that is

$$\delta = -\frac{\Re(W_{cyc})}{2E_{modal}}. \quad (3)$$

The modal work per cycle  $\Re(W_{cyc})$  is calculated from the unsteady pressure field on the blade surface and the blade velocity. The modal energy  $E_{modal}$  is calculated with complex amplitude of the blade mode deformation, the angular frequency, and the modal mass.

$$E_{modal} = \frac{1}{2} \omega^2 \tilde{\mathbf{x}}^H M_{modal} \tilde{\mathbf{x}} \quad (4)$$

The solver allows a unidirectional flutter simulation with direct coupling of the intake domain, rotor, stator, and far field. The solver is able to transfer unsteady pressure distribution between rotating and stationary domain. This is achieved by decomposing the unsteady pressure at the interface with a circumferential Fourier decomposition and transferring it to the other domain. More details about the implementation and used boundary condition of the solver can be found in [19]. The unsteady coupling of different domains can either be activated or deactivated. To extract the influence of the intake reflection on the aerodynamic damping, the simulation are performed with and without coupling (referred to as "no reflection" below). The interfaces, inlet, and outlet feature a Giles 2D non-reflecting boundary condition, based on circumferential mode decomposition at generated radial bands, [20]. Phase lag boundary condition allow the simulation of only one blade passage, which reduces the computational cost compared to a full wheel simulation. The numerical domain is visualized in Fig. 3. Intake length to diameter of  $l/d = 0.36$  and  $0.59$  are analyzed in this study. Boundary parameters are defined for the inlet (1), the outlet of the wind tunnel (2), and the outlet behind the stator (5). An interface is defined between the intake domain and rotor domain (3-I) as well as rotor domain and stator domain (4-I). The wind tunnel wall is treated as an inviscid wall and is close to the actual wind tunnel geometry. The rotor and stator domain are meshed with *AutoGrid*. The intake, the wind tunnel, and the spinner is meshed in *ANSYS ICEM*, using a butterfly topology to mesh the spinner up to the axis of rotation at  $r = 0$  mm. Important numerical settings are described in Tab. 2. Second order spatial discretization and the Fromm scheme in combination with the van Albada limiter are used. The

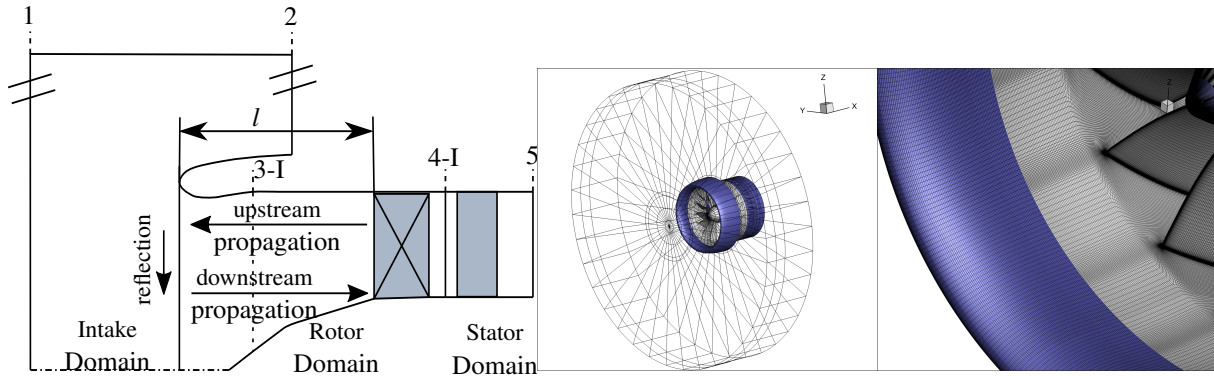


FIGURE 3. VISUALIZATION OF CFD DOMAIN

TABLE 2. NUMERICAL SETTINGS

Setting	Flutter Simulation
Mode	HB
Wall treatment	Low-Reynolds
Inlet	$p_{t,1}, T_{t,1}, \beta_1, \beta'_1, l, I, Ma$
Outlet	$p_5$
Outlet wind tunnel	$p_2$
Turbulence model	$k-\omega$
Transition model	$\gamma-Re\Theta$
$y^+$	$\approx 1$
No. of Harmonics	0 + 1
Vibration Amplitude	0.1 mm

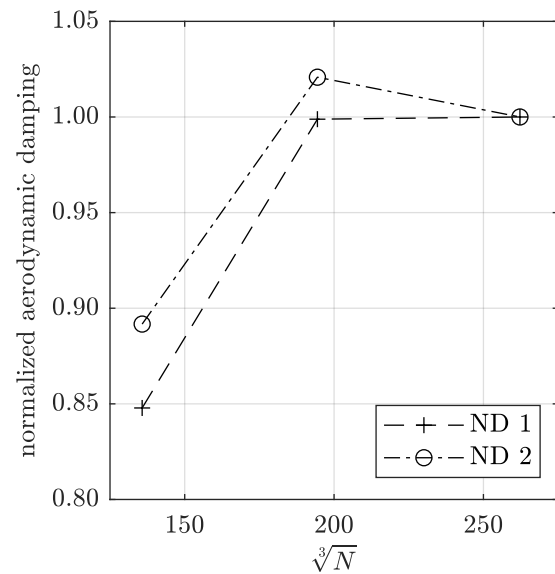


FIGURE 4. MESH STUDY AT OPERATING CONDITION A

low Reynolds wall treatment is used, thus the viscous sublayer is resolved by the numerical mesh. The unsteady turbulence and transition effects are included. The mean flow (0th harmonic) and the 1st harmonic of the blade vibration frequency is resolved in the simulation. The simulation is restarted based on a converged steady-state simulation, with a ramped CFL number up to 10 within the first 300 steps after the restart. The required mesh density was determined using the grid convergence index (GCI) to ensure mesh independent results [21]. With a maximum GCI of about 0.014% for the mass flow rate, the results can be stated as mesh independent. For operating condition A, a mesh study has also been performed regarding the aerodynamic damping of ND 1 and ND 2. The normalized aerodynamic damping is plotted over the number of nodes in Fig. 4. It is noticeable, that for ND 1 a very good grid convergence is achieved between the middle ( $\sqrt[3]{N} = 194$ ) and the fine mesh ( $\sqrt[3]{N} = 262$ ). For ND 2

the middle and fine mesh are still close in aerodynamic damping, but not in an asymptotic trend. However, the variation with 2% (0.1 percentage point in log. decrement) is accepted and the middle mesh is used in this work. Depending on the intake length the mesh consists of 7.35 million ( $l/d = 0.36$ ) and 7.47 million ( $l/d = 0.59$ ) cells.

### Structural approach

To analyze the response of the blade for different layups and rotational speeds, a modal analysis is performed using the Lanczos method from *Nastran* solution 103. This is the default setup for performing a modal analysis with *Nastran* and delivers accurate results for most problems. Due to the simplicity of the used model there is no need to investigate other solvers. The

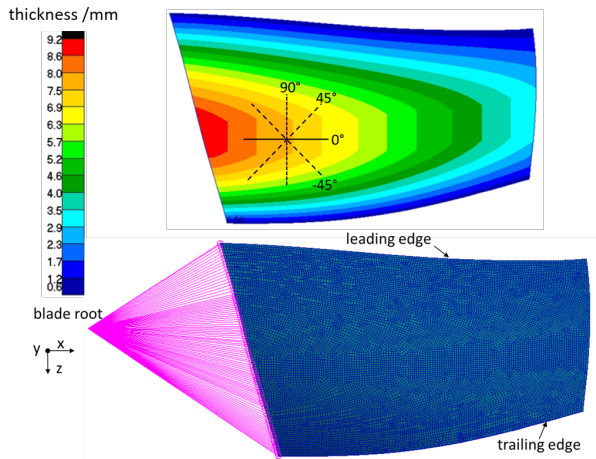


FIGURE 5. FEM SETUP

FE model for the analysis is created with *Patran 2012.2.2* using shell elements with the respective composite properties. The geometry for the modal analysis represents the blades "hot shape" meaning the shape it will take during design load conditions (8667 RPM and 63.35 kg/s mass flow rate). The modal analysis is performed for rotational speeds from 0 RPM to 9500 RPM in steps of 500 RPM to achieve a Campbell diagram with sufficient granularity. The model is shown at the bottom of Fig. 5. The root part of the model is constrained with a rigid RBE2 multi-point-constraint (MPC), which prevents the movement of the nodes and provides the stiffness needed to simulate the clamping of the blades at the hub. The composite blades are physically clamped at the root by means of suitable metallic parts (frame and wedge). The entire root is inserted and clamped. These fixed constraints have been verified by past experiences (propeller design: FP7 - LOSITA, H2020 - POLITE, H2020 - ERACLE) using the same design of the joint. The rotational forces are introduced through the *Nastran* RFORCE card. With the given density and volume of the parts and a "fictional" rotation speed the resulting forces are calculated and distributed over the nodes.

The color plot in Fig. 5 shows the thickness distribution of the blade in mm and the convention for the orientation of the different layers.

## RESULTS

### Analysis of lay-up-variations

The composite blade allows the variation of structural dynamic parameters, without the need to change the geometry of the blade itself. This is either achieved by changing the material or the lay-up of the plies. In this work, the material is kept constant and only the lay-up is varied. A reference blade design made of titanium alloy Ti-6Al-4V material with the same geometry is also investigated and compared to the different composite

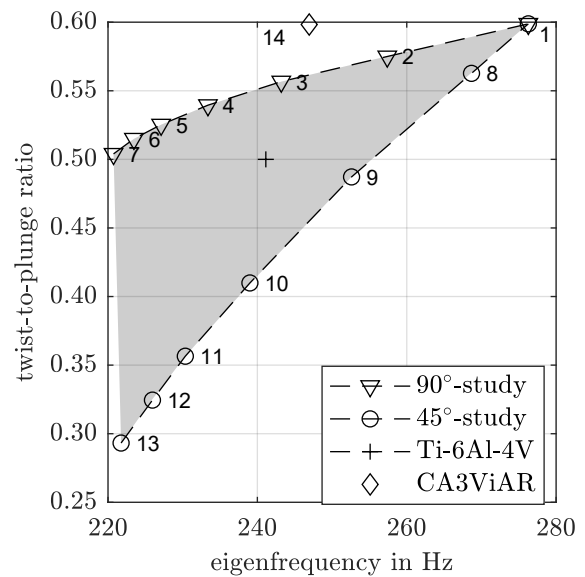


FIGURE 6. STRUCTURAL DYNAMIC PARAMETERS (MODE 1) OF COMPOSITE LAY-UPS WITH MTC510 MATERIAL AND Ti-6Al-4V BLADE

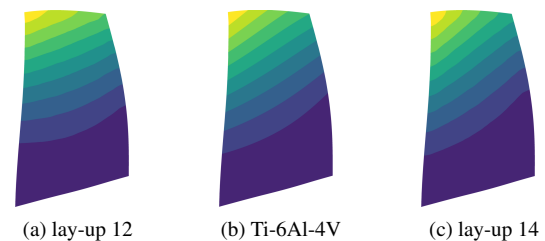
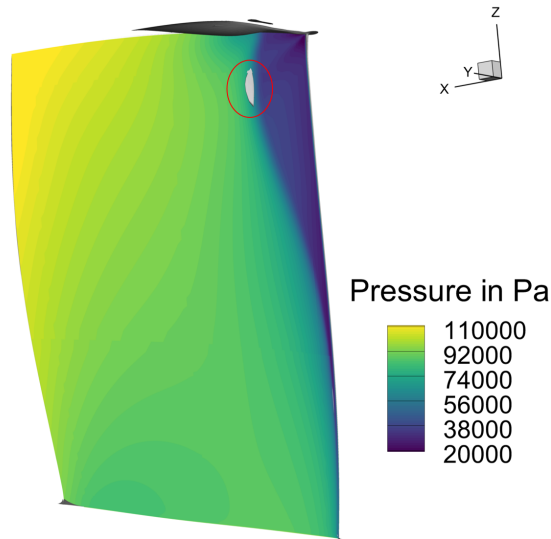


FIGURE 7. MODE SHAPES OF DIFFERENT BLADE DESIGNS, MODE 1

lay-ups. Starting from a baseline ply lay-up (Fig. 6 lay-up 1), sensitivity studies have been performed by replacing  $0^\circ$  plies with  $90^\circ$  plies (Fig. 6 "▽") to lower the frequency of the 1st bending mode or  $\pm 45^\circ$  plies (Fig. 6 "○") to lower the twist-to-plunge ratio while also lowering the eigenfrequency of the 1st bending mode. The lay-ups of the according blade designs are given in Tab. 3. The maximum number of plies for all lay-ups is 62. Due to the symmetry "s" of the lay-ups only half of the plies are given.

The lay-up modifications are beginning from the outer  $0^\circ$  plies moving to the middle of the blade. Changes to the outer plies have the largest effect since the overall ply size is decreased towards the middle of the blade and the distance to the neutral axis and therefore the influence on the bending stiffness is the largest for the outer plies.

It is noticeable that replacing  $0^\circ$  plies with  $90^\circ$  plies especially in



**FIGURE 8.** SURFACE PRESSURE AND FLOW SEPARATION (GREY) ON ROTOR BLADE SUCTION SIDE IN OPERATING CONDITION A

the beginning (Fig. 6, lay-ups 1-4) results in a drastic reduction of the eigenfrequency for the 1st bending mode. This is because  $0^\circ$  plies offer the highest bending stiffness while  $90^\circ$  plies offer the lowest. This effect is slightly damped by keeping a  $0^\circ$  ply between every double stack of  $90^\circ$  plies to retain a feasible lay-up. Due to this regulation, the lowest eigenfrequency is not much lower than the result of the  $45^\circ$ -study since it does not require the intermediate  $0^\circ$  ply due to the alternating lay-up. With increasing amount of  $90^\circ$  plies, the twist-to-plunge ratio is slightly lowered as well. This is more to the fact that the lower bending stiffness increases the plunge than the  $90^\circ$  plies having an effect on the torsional stiffness of the blade. The  $\pm 45^\circ$  plies offer a bending stiffness in between that of  $0^\circ$  plies and  $90^\circ$  plies and the largest possible torsional stiffness. By replacing  $0^\circ$  plies with  $\pm 45^\circ$  plies, the bending stiffness decreases and the torsional stiffness increases leading to a drastic drop in both twist-to-plunge ratio and eigenfrequency of the 1st bending mode.

The studies performed with  $90^\circ$  plies and  $45^\circ$  plies set the boundaries of a field of eigenfrequency/twist-to-plunge ratio combinations that can be reached by lay-ups combining variations of those plies (shaded area in Fig. 6). Within CA3ViAR, the blade is especially designed to generate flutter at throttled fan conditions. To achieve this an eigenfrequency/twist-to-plunge ratio combination outside of that field is required. This is achieved by changing the angle of the outer plies from  $\pm 45^\circ$  to  $\pm 70^\circ$  of the lay-up 2. This results in lay-up 14, with its structural dynamic parameters shown in Fig. 6. The CA3ViAR design has an eigenfrequency of 246.9 Hz and a twist-to-plunge ratio 0.598. For comparison, Fig. 6 also provides the results of a blade made

of Ti-6Al-4V alloy (“+” sign; an eigenfrequency of 241.1 Hz and a twist-to-plunge ratio of 0.5).

The resulting aerodynamic damping of the composite designs and the Ti-6Al-4V blade are shown in Fig. 9 for the operating condition point A (see Fig. 2). The operating condition point A is unstable for several blade designs (Mode 1, ND 1 and 2) and therefore, chosen for this study. The surface pressure and flow separation of point A are shown in Fig 8. The footprint of the shock is clearly identified close to the leading edge. A small separated area is found downstream of the shock at 92% span. However, no large separated areas are present. The aerodynamic damping is simulated with the short intake design ( $l/d = 0.36$ ) and coupling between the intake domain, the rotor domain, and the stator domain. To analyze the effect of the intake reflections on the aerodynamic damping, the simulations are repeated without intake domain coupling (“no reflection” in Fig. 9).

For the composite blade designs at ND 1, shown in Fig. 9a, the aerodynamic damping without the intake coupling is decreasing with added  $90^\circ$  plies (lay-up 2-7,  $\nabla$ ). Here, the reduction in reduced frequency predominates the decrease in twist-to-plunge ratio. However, by adding  $45^\circ$  plies to the lay-ups (8-13,  $\circ$ ), the aerodynamic damping is increased significantly, despite a similar decrease in reduced frequency compared to the lay-ups with added  $90^\circ$  plies. Without intake reflections, blade designs with lay-up 10-13 are stable at point A and ND 1. Considering the reflections of the short intake, the rotor is destabilized compared to simulations without the intake reflections for all blade designs. However, the lay-ups 11-13 retain stability considering intake reflections.

In Fig. 9b the resulting aerodynamic damping of ND 2 is plotted for the different composite blade designs. Similar to ND 1, the aerodynamic damping can be increased by adding  $45^\circ$  plies to the lay-up (lay-up 8-13,  $\circ$ ). For ND 2, it is noticeable that the intake reflections are of major concern regarding the stability of the rotor blade. In this case, the reflected wave is close to the maximum destabilization at a reduced frequency of 0.89. This is shown in Fig. 10. Here, the phase difference of up- and downstream traveling wave is close to  $90^\circ$  for a maximum destabilization, which is in line with the observation in [2]. The phase difference is extracted using a radial mode analysis, accordingly to the procedure described in [22]. The unsteady pressure on two axial planes located at 10 mm and 20 mm upstream of the rotor domain is used to decompose the up- and downstream traveling acoustic modes with a circumferential mode order of 2. It is noticeable that due to the change in blade frequency and thereby the axial wavelength of the induced acoustic mode, the phase difference of up- and downstream traveling wave at the rotor is shifted. This reduces the intake driven influence on aerodynamic damping ( $\Delta\delta = \delta_{coupled} - \delta_{noreflexion}$ ) to only a small influence at reduced frequencies of 0.72. The effect of decreased destabilizing intake coupling is also present for the  $90^\circ$ -study. The  $45^\circ$ -study accomplishes a stable blade design with the influence by the in-

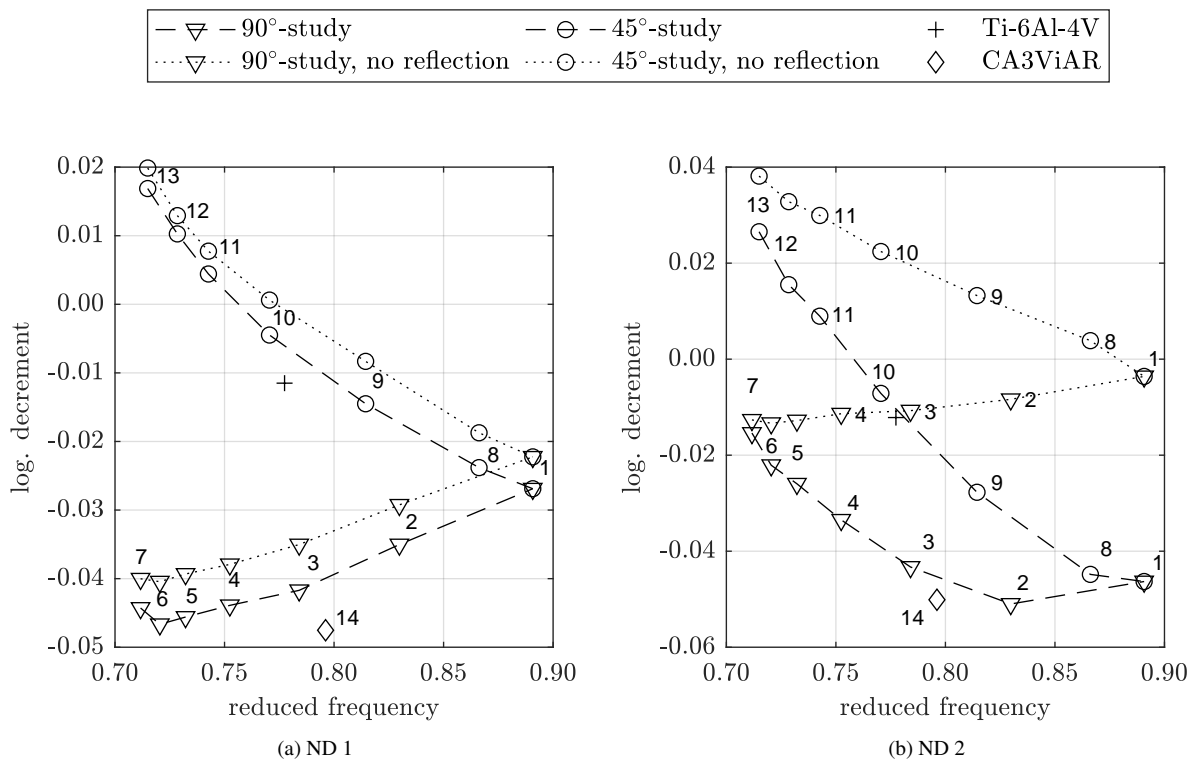


**FIGURE 9.** AERODYNAMIC DAMPING OF DIFFERENT BLADE DESIGNS AT POINT A (100 Nn, 53.8 kg/s), SHORT INTAKE

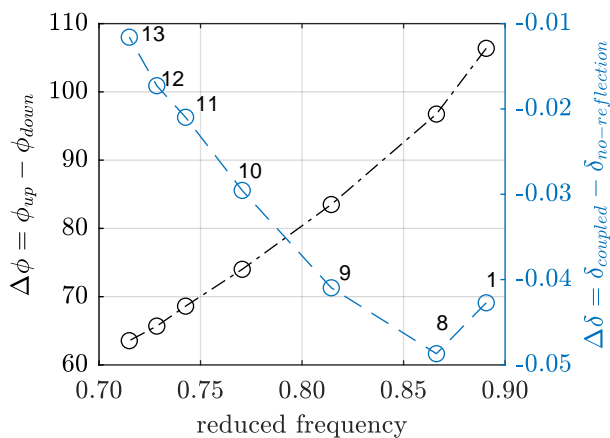


**FIGURE 10.** PHASE DIFFERENCE OF UP- AND DOWNSTREAM TRAVELING WAVE AND INFLUENCE ON AERODYNAMIC DAMPING OVER REDUCED FREQUENCY OF 45° STUDY

take, due to the increase of the rotor-only damping based on the lowered twist-to-plunge ratio and the decreased destabilizing by the intake reflections at lowered blade frequencies. The lay-ups 11-13 are stable in operating condition A.

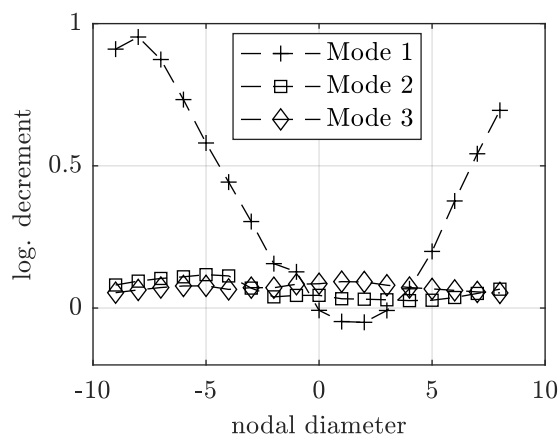


**FIGURE 11.** AERODYNAMIC DAMPING OVER NODAL DIAMETER OF DIFFERENT MODES IN OPERATING POINT A, CA3ViAR DESIGN, SHORT INTAKE

This shows the potential composite materials offer to influence the rotor-only damping and the coupling with the intake. The reduction in twist-to-plunge ratio due to added 45° plies increases the rotor-only damping for ND 1 and ND 2 significantly. The possible range in eigenfrequency is able to reduce the destabi-



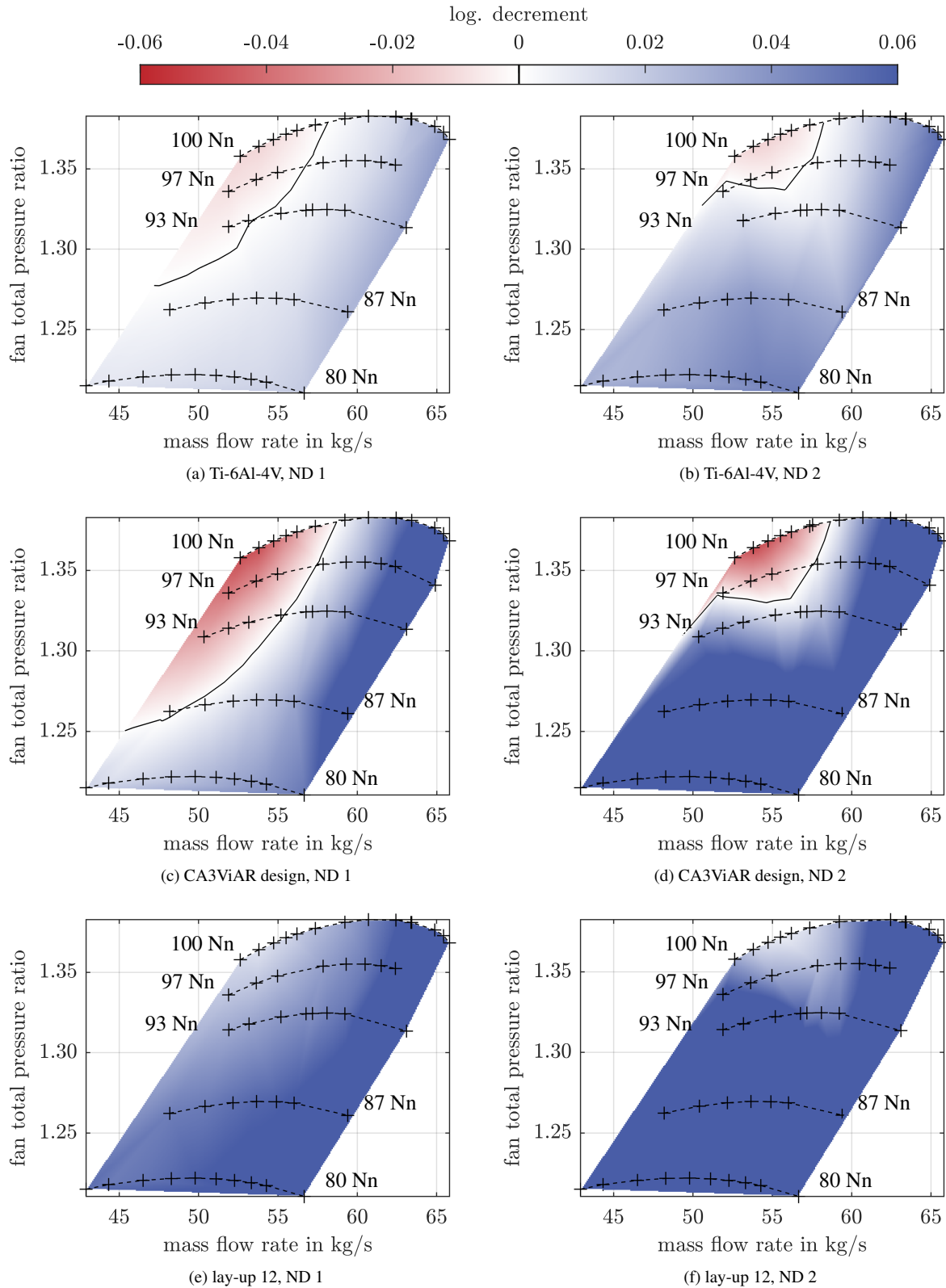


**FIGURE 12.** STABILITY MAP OF DIFFERENT BLADE DESIGNS FOR MODE 1, ND 1 AND ND 2, COUPLED WITH SHORT INTAKE

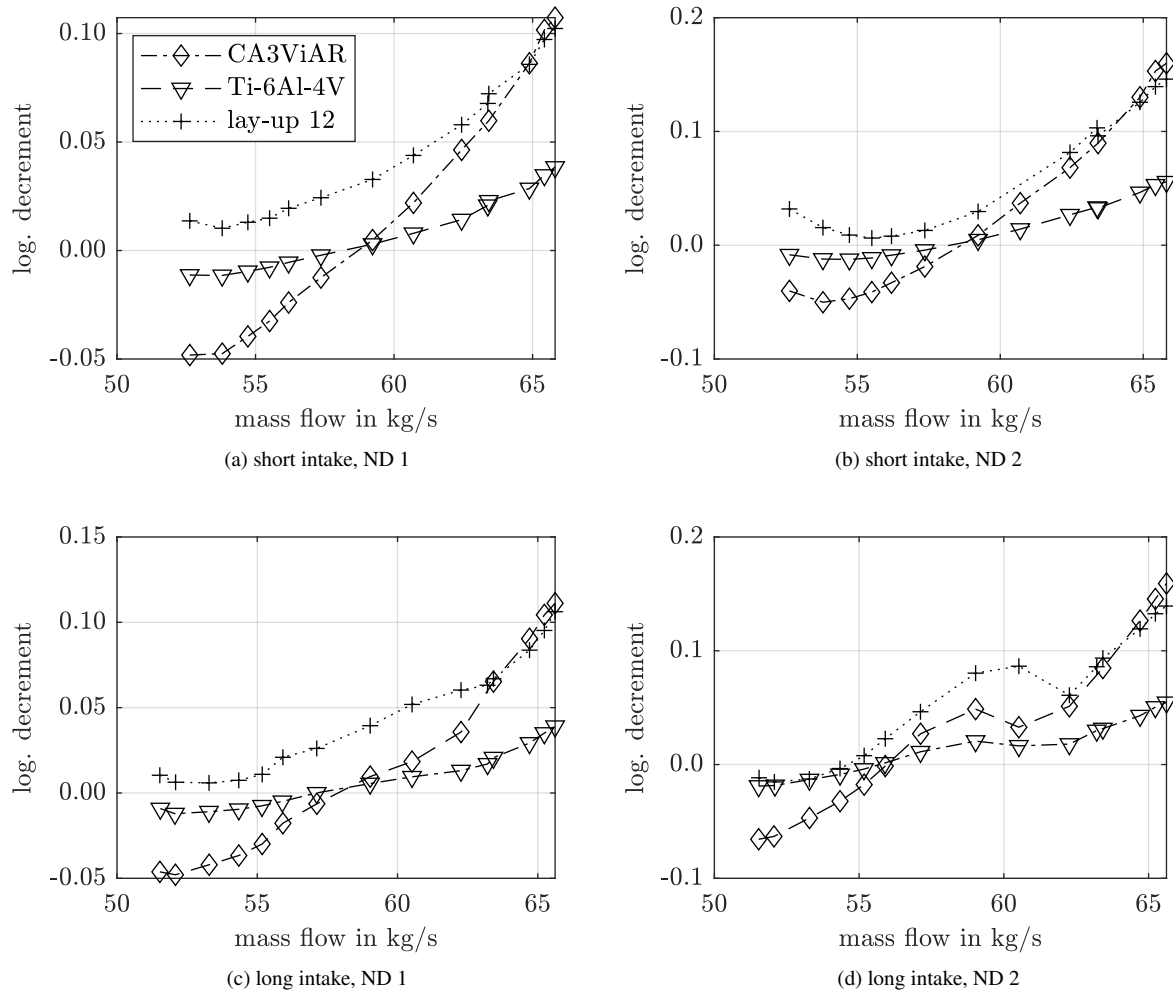


**FIGURE 13.** AERODYNAMIC DAMPING OVER MASS FLOW RATE AT 100 Nn

lizing influence of the intake from maximum destabilization to nearly no influence. The CA3ViAR blade (lay-up 14) is designed to have a margin in negative aerodynamic damping at operating condition A to overcome mechanical damping and the stabilizing influence of mistuning. The negative damping is -5.01% for ND 2. Figure 11 shows the resulting aerodynamic damping over the nodal diameter up to the 3rd Mode for operating point A.

### Stability map of different blade designs

The lay-up 12 is depicted to analyze its stability for different operating conditions and intake length. This lay-up is stable for point A in the layup study with intake reflection. Furthermore, the resulting aerodynamic damping is compared to the titanium alloy Ti-6Al-4V reference blade and the CA3ViAR design (lay-up 14).

In Fig. 12, the stability map for ND 1 and ND 2 for these three

blade designs are shown for rotational speeds from 80% to 100% speed. The data between the simulated points is interpolated linearly. The Ti-6Al-4V reference blade design shows unstable areas for ND 1 and ND 2 in the top left corner of the performance map. Comparing the amplitude of aerodynamic damping for all operating points of the titanium alloy blade to the composite blades, it is noticeable that slope and absolute aerodynamic damping are reduced. This is due to the increased modal mass of the titanium alloy blade compared to the lighter composite blades, leading to a decreased aerodynamic damping amplitude for the same aerodynamic work, which is described in Eq. 3 and 4. This is distinct in the stability map of the CA3ViAR design, shown in Fig. 12c and 12d. Despite the larger unstable areas and negative aerodynamic damping, the CA3ViAR design retains a sufficient stability margin at normal operating conditions (e.g. design point and take-off).

The stability map of lay-up 12 coupled with the short intake ( $l/d = 0.36$ ) shows only stable operating condition over the points analyzed. The minimal aerodynamic damping is 0.63% at 100% speed and 55.5 kg/s for ND 2. Similar to the other stability maps, the area with the lowest aerodynamic damping is at throttled condition for high rotational speeds. Due to the lowered blade eigenfrequency the coupling with the short intake is reduced, especially for ND 2.

In Fig. 13, the aerodynamic damping of the different designs over the mass flow rate at 100% speed is plotted in detail for both short ( $l/d = 0.36$ ) and long intake ( $l/d = 0.59$ ) designs. For the short intake and ND 2 (Fig. 13b), throttling the fan to mass flow rates below 55 kg/s does not further decrease the aerodynamic damping. This is due to the reduction in axial Mach number that increases the axial wavelength and thereby shift the phase lag between up- and downstream traveling waves. With lower eigenfrequency of the blade design, the point with a positive slope of damping is shifted to higher mass flow rates. This allows the blade design with lay-up 12 to remain stable, since the rotor-only damping is sufficient high at these higher mass flow rates to overcome the maximum destabilization by the intake reflections. The frequency of the CA3ViAR design is chosen for a destabilizing coupling with the intake to achieve a margin in negative aerodynamic damping. This is done to overcome mechanical damping and the stabilizing effect of mistuning to allow flutter measurements within the wind tunnel operating points. In this case, a higher eigenfrequency would lead to problems with the EO crossing. For the long intake and ND 2, the destabilizing intake coupling is increased for the designs with lower blade frequency due to the shift in relative phase of up- and downstream traveling waves by the increased propagation length. Therefore, the point with maximum destabilization by the long intake is at an operating condition with lower mass flow rate and thus with lower rotor-only damping. This leads to unstable conditions for the blade design with lay-up 12 at mass flow rates below 54.5 kg/s. The destabilizing coupling for both CA3ViAR and Ti-6Al-4V blade design is increased for these operating conditions with the long intake, leading to a minimal aerodynamic damping of -6.6% for the CA3ViAR design.

## CONCLUSIONS

In this paper, different composite blades are designed using lay-up variations and compared regarding their aerodynamic damping and with a reference titanium alloy blade of the same geometry. The coupling with the intake reflections is incorporated within the numerical simulation and different intake length are analyzed and compared to the rotor-only damping. The main conclusions are:

- The variation of the orientation of the plies within the composite lay-up allows a wide variation in eigenfrequency and

twist-to-plunge ratio, which are both important parameters for the aerodynamic damping.

- The rotor-only damping and the coupling with the intake can be significantly influenced by the chosen lay-up.
- A blade geometry, which has unstable operating condition for a titanium alloy (Ti-6Al-4V) reference blade is stabilized for all operating conditions of interest with a short intake typical of UHBR designs using a lay-up with reduced eigenfrequency and twist-to-plunge ratio. The minimal damping is 0.63%. Furthermore, for the special requirement in the CA3ViAR project, i.e. to measure flutter instabilities within the wind tunnel operation, a lay-up is found that generates negative aerodynamic damping up to -6.6%. These studies show that the blade lay-up should be considered during the design process not only to achieve high stiffness and strength, but also to generate a stable fan blade design and by that extend the fan performance map.
- It is shown that, compared to a titanium alloy blade, the composite blades have a higher amplitude and slope in aerodynamic damping. This should be considered during flutter experiments during wind tunnel operation.
- For the given fan, lengthening the intake from  $l/d = 0.36$  to  $l/d = 0.59$  results in a decrease of aerodynamic damping at throttled fan condition at 100% speed.

## ACKNOWLEDGMENTS

This project has received funding from the Clean Sky 2 Joint Undertaking (JU) under grant agreement No 864256. The JU receives support from the European Union's Horizon 2020 research and innovation programme and the Clean Sky 2 JU members other than the Union. This is gratefully acknowledged by the authors. Furthermore, the authors would like to acknowledge the German Aerospace Center (Deutsches Zentrum für Luft- und Raumfahrt, DLR) for providing TRACE. The authors also would like to thank Niklas Maroldt from Leibniz University Hannover for valuable discussion and his contributions.

## DISCLAIMER

The present work reflects only the authors' view and the European Commission and Clean Sky 2 JU are not responsible for any use that may be made of the information contained in this paper.

## REFERENCES

- [1] Lee, K.-B., Wilson, M., and Vahdati, M., 2017. "Numerical study on aeroelastic instability for a low-speed fan". *Journal of Turbomachinery*, **139**(7), p. 68.
- [2] Vahdati, M., Smith, N., and Zhao, F., 2015. "Influence of

- intake on fan blade flutter”. *Journal of Turbomachinery*, **137**(8), p. 54.
- [3] Vahdati, M., Sayma, A. I., Marshall, J. G., and Imregun, M., 2001. “Mechanisms and prediction methods for fan blade stall flutter”. *Journal of Propulsion and Power*, **17**(5), pp. 1100–1108.
- [4] Srinivasan, A. V., 1997. “Flutter and resonant vibration characteristics of engine blades”. *Journal of Engineering for Gas Turbines and Power*, **119**(4), pp. 742–775.
- [5] Vahdati, M., and Cumpsty, N., 2016. “Aeroelastic instability in transonic fans”. *Journal of Engineering for Gas Turbines and Power*, **138**(2), p. 945.
- [6] Nipkau, J., Power, B., and Jordan, M., 2017. “Aeromechanical design and test of a modern highly loaded fan”. In Volume 2B: Turbomachinery, American Society of Mechanical Engineers.
- [7] Vahdati, M., Simpson, G., and Imregun, M., 2011. “Mechanisms for wide-chord fan blade flutter”. *Journal of Turbomachinery*, **133**(4), p. 54.
- [8] Zhao, F., Smith, N., and Vahdati, M., 2017. “A simple model for identifying the flutter bite of fan blades”. *Journal of Turbomachinery*, **139**(7), p. 041029.
- [9] Vahdati, M., Lee, K.-B., and Sureshkumar, P., 2020. “A review of computational aeroelasticity of civil fan blades”. *International Journal of Gas Turbine, Propulsion and Power Systems*, **11**(4), pp. 22–35.
- [10] Schnell, R., and Frey, C., 2021. “Acoustic impact on fan flutter characteristics in short aero engine intakes”. In AIAA AVIATION 2021 FORUM, American Institute of Aeronautics and Astronautics.
- [11] Panovsky, J., and Kielb, R. E., 2000. “A design method to prevent low pressure turbine blade flutter”. *Journal of Engineering for Gas Turbines and Power*, **122**(1), pp. 89–98.
- [12] Figaschewsky, F., Kühhorn, A., Beirow, B., Nipkau, J., Giersch, T., and Power, B., 2017. “Design and analysis of an intentional mistuning experiment reducing flutter susceptibility and minimizing forced response of a jet engine fan”. In Volume 7B: Structures and Dynamics, American Society of Mechanical Engineers.
- [13] Stapelfeldt, S., and Vahdati, M., 2019. “Improving the flutter margin of an unstable fan blade”. *Journal of Turbomachinery*, **141**(7).
- [14] Reiber, C., and Blocher, M., 2017. “Potential of aeroelastic tailoring to improve flutter stability of turbomachinery compressor blades”. In *Proceedings of 12th European Conference on Turbomachinery Fluid dynamics & Thermodynamics*.
- [15] Eggers, T., Friedrichs, J., Goessling, J., Seume, J. R., Natale, N., Flüh, J. P., and Paletta, N., 2021. “Composite UHBR fan for forced response and flutter investigations”. In Volume 2A: Turbomachinery — Axial Flow Fan and Compressor Aerodynamics, American Society of Mechanical Engineers.
- [16] Paletta, N., Flüh, J., Lindemann, J., Seume, J., Goessling, J., Friedrichs, J., Eggers, T., Russo, S., Natale, N., Vlachos, D., Mazarakos, D., Baltopoulos, A., and Vavouliotis, A., 2022. “The preliminary design of a scaled composite UHBR fan for a wind tunnel test campaign”. *IOP Conference Series: Materials Science and Engineering*, **1226**(1), p. 012041.
- [17] Cumpsty, N. A., 2010. “Preparing for the future: Reducing gas turbine environmental impact—igti scholar lecture”. *Journal of Turbomachinery*, **132**(4).
- [18] Frey, C., Ashcroft, G., Kersken, H.-P., and Voigt, C., 2014. “A harmonic balance technique for multistage turbomachinery applications”. American Society of Mechanical Engineers Digital Collection.
- [19] Frey, C., Ashcroft, G., and Kersken, H.-P., 2015. “Simulations of unsteady blade row interactions using linear and non-linear frequency domain methods”. In Volume 2B: Turbomachinery, American Society of Mechanical Engineers.
- [20] Kersken, H.-P., Ashcroft, G., Frey, C., Wolfrum, N., and Korte, D., 2014. “Nonreflecting boundary conditions for aeroelastic analysis in time and frequency domain 3d rans solvers”. In Volume 2B: Turbomachinery, American Society of Mechanical Engineers.
- [21] Celik, I. B., Ghia, U., Roache, P. J., and Freitas, C. J., 2008. “Procedure for estimation and reporting of uncertainty due to discretization in cfd applications”. *Journal of fluids Engineering-Transactions of the ASME*.
- [22] Mumcu, A., Keller, C., Hurfar, C. M., and Seume, J. R., 2016. “An acoustic excitation system for the generation of turbomachinery specific sound fields: Part i — design and methodology”. In Volume 2A: Turbomachinery, American Society of Mechanical Engineers.

**TABLE 3. HIGHLIGHTED LAY-UPS**

I	lay-up
1	$[45^\circ, -45^\circ, 0^\circ]_S$
2	$[45^\circ, -45^\circ, 90^\circ, 90^\circ, 0^\circ]_S$
3	$[45^\circ, -45^\circ, 90^\circ, 90^\circ, 0^\circ, 90^\circ, 90^\circ, 0^\circ, 0^\circ, 0^\circ, 0^\circ, 0^\circ, 0^\circ, 0^\circ, 0^\circ, 0^\circ, 0^\circ, 0^\circ, 0^\circ, 0^\circ, 0^\circ, 0^\circ, 0^\circ, 0^\circ]_S$
4	$[45^\circ, -45^\circ, 90^\circ, 90^\circ, 0^\circ, 90^\circ, 90^\circ, 0^\circ, 90^\circ, 90^\circ, 0^\circ, 0^\circ, 0^\circ, 0^\circ, 0^\circ, 0^\circ, 0^\circ, 0^\circ, 0^\circ, 0^\circ, 0^\circ, 0^\circ, 0^\circ, 0^\circ]_S$
5	$[45^\circ, -45^\circ, 90^\circ, 90^\circ, 0^\circ, 90^\circ, 90^\circ, 0^\circ, 90^\circ, 90^\circ, 0^\circ, 90^\circ, 90^\circ, 0^\circ, 0^\circ, 0^\circ, 0^\circ, 0^\circ, 0^\circ, 0^\circ, 0^\circ, 0^\circ, 0^\circ, 0^\circ]_S$
6	$[45^\circ, -45^\circ, 90^\circ, 90^\circ, 0^\circ, 90^\circ, 90^\circ, 0^\circ, 90^\circ, 90^\circ, 0^\circ, 90^\circ, 90^\circ, 0^\circ, 90^\circ, 90^\circ, 0^\circ, 0^\circ, 0^\circ, 0^\circ, 0^\circ, 0^\circ, 0^\circ, 0^\circ]_S$
7	$[45^\circ, -45^\circ, 90^\circ, 90^\circ, 0^\circ, 90^\circ, 90^\circ, 0^\circ, 90^\circ, 90^\circ, 0^\circ, 90^\circ, 90^\circ, 0^\circ, 90^\circ, 90^\circ, 0^\circ, 90^\circ, 90^\circ, 0^\circ, 0^\circ, 0^\circ, 0^\circ, 0^\circ]_S$
8	$[45^\circ, -45^\circ, 45^\circ, -45^\circ, 0^\circ]_S$
9	$[45^\circ, -45^\circ, 45^\circ, -45^\circ, 45^\circ, -45^\circ, 45^\circ, -45^\circ, 0^\circ, 0^\circ, 0^\circ, 0^\circ, 0^\circ, 0^\circ, 0^\circ, 0^\circ, 0^\circ, 0^\circ, 0^\circ, 0^\circ, 0^\circ, 0^\circ, 0^\circ, 0^\circ]_S$
10	$[45^\circ, -45^\circ, 45^\circ, -45^\circ, 45^\circ, -45^\circ, 45^\circ, -45^\circ, 45^\circ, -45^\circ, 45^\circ, -45^\circ, 0^\circ, 0^\circ, 0^\circ, 0^\circ, 0^\circ, 0^\circ, 0^\circ, 0^\circ, 0^\circ, 0^\circ, 0^\circ, 0^\circ]_S$
11	$[45^\circ, -45^\circ, 45^\circ, -45^\circ, 45^\circ, -45^\circ, 45^\circ, -45^\circ, 45^\circ, -45^\circ, 45^\circ, -45^\circ, 45^\circ, -45^\circ, 0^\circ, 0^\circ, 0^\circ, 0^\circ, 0^\circ, 0^\circ, 0^\circ, 0^\circ, 0^\circ, 0^\circ]_S$
12	$[45^\circ, -45^\circ, 45^\circ, -45^\circ, 45^\circ, -45^\circ, 45^\circ, -45^\circ, 45^\circ, -45^\circ, 45^\circ, -45^\circ, 45^\circ, -45^\circ, 45^\circ, -45^\circ, 45^\circ, -45^\circ, 0^\circ, 0^\circ, 0^\circ, 0^\circ, 0^\circ, 0^\circ, 0^\circ]_S$
13	$[45^\circ, -45^\circ, 45^\circ, -45^\circ, 45^\circ, -45^\circ, 45^\circ, -45^\circ, 45^\circ, -45^\circ, 45^\circ, -45^\circ, 45^\circ, -45^\circ, 45^\circ, -45^\circ, 45^\circ, -45^\circ, 45^\circ, -45^\circ, 45^\circ, -45^\circ, 45^\circ, -45^\circ, \dots$ $-45^\circ, 45^\circ, -45^\circ, 0^\circ]_S$
14	$[70^\circ, -70^\circ, 90^\circ, 90^\circ, 0^\circ]_S$